

High resolution large working distance scanning helium microscopy

SM Lambrick^{a,d,*}, NA von Jeinsen^a, A Radić^a, DJ Ward^{a,b}, D MacLaren^c, AP Jardine^a

^a*Cavendish Laboratory, University of Cambridge, JJ Thompson Avenue, Cambridge, CB3 0US, UK*

^b*Ionoptika Ltd., Unit B6, Millbrook Close, Chandler's Ford, SO53 4BZ, UK*

^c*SUPA, School of Physics & Astronomy, University of Glasgow, Glasgow, G12 8QQ, UK*

^d*ISIS Facility, Rutherford Appleton Laboratory, Chilton, Didcot, Oxfordshire, OX11 0QX, UK*

Abstract

Scanning helium microscopy (SHeM) is attractive for imaging delicate and insulating surfaces because it combines a non-destructive neutral-atom probe with strong surface sensitivity. However, large-working-distance pinhole instruments have so far been limited in spatial resolution. Here we report sub-micron resolution in a large-working-distance pinhole SHeM, with an intrinsic beamwidth of 340 nm achieved at working distances of 770 μm to 850 μm . This sixfold improvement over our previous long-working-distance configuration is enabled by constrained optimisation of the atom optics together with a redesigned high-resolution pinhole-plate, a reduced pinhole diameter, an increased source–pinhole distance and a larger detector aperture. Beamwidth measurements agree well with the modified optimisation model and show that geometric, source-size and diffraction terms now contribute on a similar footing, placing the instrument in a near-optimised regime. The resulting combination of sub-micron beam size, useful depth of field and practical sample access is demonstrated on bacterial specimens and eroded diamond. The work establishes large-working-distance pinhole SHeM as a viable sub-micron imaging platform and extends its usefulness for topographic imaging and micro-diffraction applications.

Keywords: Scanning Helium Microscopy, Neutral Atom Microscopy, Helium Atom Scattering, Resolution, Optimisation

1. Introduction

High-resolution surface microscopy is not defined solely by the ability to form a small probe. In practice, useful resolving power depends on the ability to recover contrast-bearing information from neighbouring regions of a specimen with sufficient signal relative to noise and background. Useful high resolution is particularly challenging for delicate, insulating, or topographically complex samples, where charged-particle techniques may suffer from beam damage, charging, or the need for conductive coatings[1, 2], while optical methods may lack the required surface specificity or spatial resolution. Scanning helium microscopy (SHeM) addresses part of this gap by using a neutral helium atom beam as a non-destructive surface probe[3, 4, 5].

SHeM forms images by rastering a sample beneath a narrow neutral helium beam and detecting the scattered flux. Because helium atoms in these instruments typically have incident energies of only 10–70 meV, they interact with the outer electronic density of the surface rather than penetrating into the material or driving the damage pathways more commonly associated with charged beams[6]. At the same time, their de Broglie wavelength, typically 0.5–2 Å, remains on the atomic scale, giving access to diffraction-based sensitivity to very small structural features[5, 7]. In practice, therefore, while the ultimate physical limit is set by the probe wavelength, the useable resolution is set by the practical atom optics and signal constraints of the

instrument. A number of SHeM instruments have been developed, and while based on similar principles, these can be broken down by their method of generating the narrow helium beam: using an active focusing zone plate[8], or using pinhole collimation, either with a large working distance[9, 10] or a short working distance[11].

The unique characteristics of helium as a microscopy probe have led to growing interest in SHeM for classes of specimen and measurement that benefit from strong surface sensitivity combined with exceptionally low probe energy. Recent work has demonstrated the utility of helium microscopy for 2D materials[10, 12, 13], biological structures[14, 15], and other samples prone to charging or beam-induced modification. Beyond topographic imaging, the same instrumental platform can also be adapted for microscopic atom-diffraction measurements[5, 7]. The combination of non-destructive imaging, surface specificity and diffraction sensitivity is one of the distinctive attractions of helium microscopy.

In addition to the spatial size of the probe useful resolution reflects the combined effect of source brightness, detection efficiency, and the the imaging or beam-forming optics that deliver signal to defined region of the sample. The implications of signal and background to practical resolution specifically for helium microscopy have been explored by Bergin et al.[16]. The first two elements are common to all microscopies, and advances in both beam generation[17, 18] and efficient detection[19] have been important in making high-performance helium microscopy experimentally viable. In the present work,

*Corresponding author: sam.lambrick@stfc.ac.uk

however, we focus on the third element: the atom-optical geometry of a large-working-distance pinhole SHeM, and the trade-offs between beam size, signal level, depth of field and practical sample access. Therefore we are concerned not only with reducing beamwidth — though beamwidth and edge-response measurements remain a key quantifiable performance metric — but with improving the experimentally useful resolving capability of large-working-distance SHeM.

To date a major limitation of large-working-distance pinhole SHeM has been spatial resolution. Sub-micron beam sizes have previously been demonstrated only in short-working-distance neutral atom microscopes[11, 20], whereas the more accessible and versatile large-working-distance instruments have generally remained in the micron-scale regime. This limitation is critical because the practical advantages of large working distance, including easier sample handling, tolerance of significant sample topography, and a larger effective depth of field, are precisely the features that make SHeM attractive for broader microscopy use. The challenge, therefore, is not simply to improve resolution, but to do so without sacrificing the sample access and flexibility that distinguish the large-working-distance geometry.

In the current work we show that the trade-off between working distance and beamwidth can be shifted substantially. We report sub-micron resolution in a large-working-distance pinhole SHeM, achieving an intrinsic beamwidth of 340 nm while maintaining working distances greater than 700 μm . This corresponds to a six-fold improvement over our previous large-working-distance configuration. The advance is enabled by combining constrained optimisation of the atom optics with a re-designed sample chamber, improved pinhole fabrication, a reduced pinhole diameter, an increased source–pinhole distance, and a compact high-resolution pinhole-plate geometry. Further we demonstrate the improved operating regime using examples from biological imaging and nanostructured materials. Thus, we establish large-working-distance pinhole SHeM as a practical sub-micron imaging platform and a more capable basis for future topographic and micro-diffraction measurements.

2. Large working distance SHeM

Several implementations of neutral-beam real-space microscopy have now been demonstrated, but they differ substantially in both atom-optical design and practical operating regime. These include the Bergen neutral atom microscope, which uses Fresnel zone-plate focusing[21, 8, 17, 22, 23], the neutral atom microscopy (NAM) developed by Witham et al. at Portland State University[11, 20], and the Cambridge[9, 24], Newcastle[25] and Hyderabad SHeMs[10] that follow the pinhole-collimation principles introduced by Barr et al.[9, 24]. Because the optical constraints and performance trade-offs are markedly different for zone-plate and pinhole instruments, the present work concerns only pinhole-collimated systems[26, 27].

The terminology in the literature is not always fully consistent: both *SHeM* and *NAM* have been used either as generic labels for helium atom imaging or as names for specific instruments. Here we use *SHeM* as the general term for scanning he-

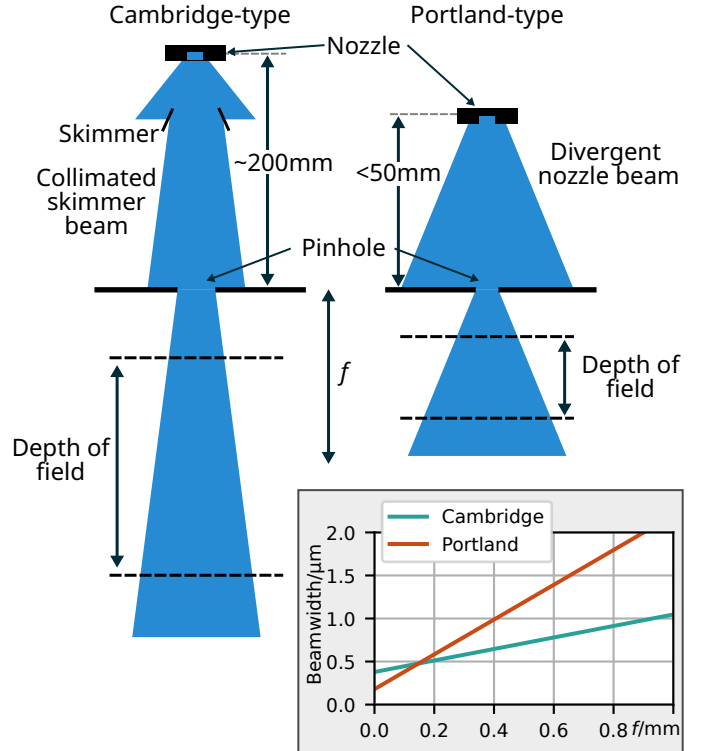


Figure 1: Basic geometry of the Cambridge-type SHeM and the Portland-type NAM. The Cambridge SHeM uses a collimated skimmer beam as its source, providing a small divergence after pinhole collimation. The Portland NAM directly uses the nozzle beam close to the pinhole, providing a large flux with a much more divergent beam. A more divergent beam will result in a smaller depth of field as the beamwidth will rapidly grow too large, as shown in the inset graph (the inset is demonstrative and does not represent any specific instrument configurations).

lium microscopy, *NAM* to refer specifically to the Portland instrument, and *Cambridge SHeM* to refer to the instrument used in the current work – the single detector Cambridge A-SHeM as introduced by Barr et al.[9]. More generally, the two pinhole-based instrument classes will be referred to as *Portland-type* and *Cambridge-type*.

A key distinction between Cambridge-type SHeM, as implemented in Cambridge, Hyderabad and Newcastle, and Portland-type NAM lies in both geometry and usability. The Portland-type NAM typically operates at short working distances ($< 100 \mu\text{m}$ and down to $30 \mu\text{m}$) in order to minimise the spot size[20], while the Cambridge-type SHeM operates at substantially larger working distances ($> 1 \text{ mm}$ previously and $> 600 \mu\text{m}$ in the current work). A simplified schematic comparison of the two geometries is shown in figure 1.

The extended working distance, f , used by the Cambridge-type SHeM confers several practical benefits to the end user: easier sample handling and mounting, compatibility with larger 3D topography, and a significantly extended depth of field. In addition, the larger distance from the nozzle to the sample leads to a more monochromatic beam[28] and hence momentum, k , resolution, allowing adaptation of the instrument for atom-diffraction measurements on microscopic sample regions[5, 7]. For a pinhole instrument, the usable depth of field is determined not only

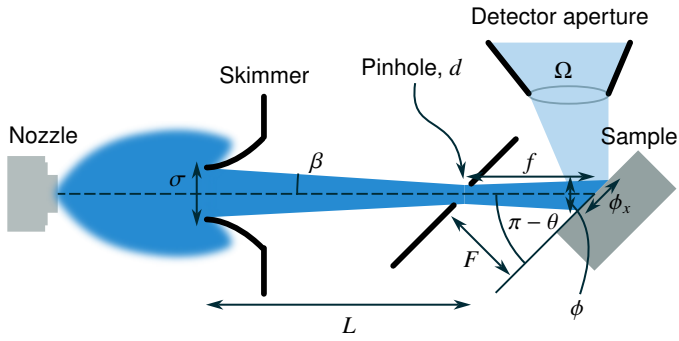


Figure 2: The optical system in the Cambridge SHeM. High pressure gas forms a supersonic expansion after passing through a nozzle into a vacuum. The centre-line of the expansion is selected by a skimmer. The beam is then passed through a pinhole aperture and is projected onto the sample, which lies at 45° to the helium beam. ϕ is the intrinsic beamwidth (perpendicular to the beam propagation direction) while ϕ_x is the beamwidth projected onto the scanning plane.

by the range of working distances over which the beamwidth remains acceptable[26], but also by the range over which sufficient signal can be maintained[29]. In this sense, large working distance is not merely a convenience of the Cambridge-type geometry, but one of its central experimental strengths. These practical advantages have, however, historically come at the expense of spatial resolution. To date, Cambridge-type SHeM implementations have generally remained restricted to resolutions $> 1 \mu\text{m}$, whereas Portland-type NAM has reported a beamwidth of 350 nm using a working distance of only $30 \mu\text{m}$ [20]. The discrepancy lies largely in the fact that earlier Cambridge-type optical configurations had not been fully optimised. The optimisation frameworks developed by Bergin et al. and Salvador-Palau et al. provide the means to address this directly[26, 30, 27], and the current work reports the realisation of the atom-optic optimisation.

3. Optical Optimisation and Trade-offs

3.1. Beam spot size

The optical system of the Cambridge SHeM is outlined schematically in figure 2. A supersonic expansion of helium is generated by exposing high pressure gas to vacuum via a narrow nozzle; the centreline of the expansion is selected by a skimmer producing a near monochromatic helium beam [31]. The beam is then passed through a pinhole, performing the final collimation and demagnification of the source. Finally, it is incident on the sample at an angle of $\theta = 45^\circ$ where the helium scattered in a particular direction is collected by a detector aperture. Key physical parameters of the system that can be changed are: the diameter of the pinhole, d , the working distance, f , the distance between the source and the pinhole, L , and the solid angle of the detector aperture, Ω . The virtual source size, σ , largely determined by the skimmer diameter in the Cambridge SHeM[32], is left fixed, and the helium wavelength is also a fixed parameter. The angular source size, β , is dependent on σ and L .

Bergin[26] and Salvador-Palau[30] identified three main contributors to the width of a helium beam at the sample in a pinhole microscope: the geometric projection of the pinhole, the demagnified source size, and diffraction through the pinhole. Both optimisation methods assume that the contributions from each of these are approximately Gaussian, giving the total beamwidth at the sample as a quadrature sum of the three contributions. Both theoretical methods considered a normal incidence microscope, however our instrument operates in a 45° incidence configuration, and therefore modifications to the mathematics are necessary. In addition, one of the key parameters of the optimisation is the angular source size, β . Unlike some other parameters, the angular source size does not directly correspond to a single physical parameter we have control over. In the current work we use a known source, with a previously measured virtual source size, and change the source–pinhole distance in order to change β . Thus, in the small angle approximation, $\beta = \sigma_{\text{source}}/L$, where L is the distance between the source and the pinhole and σ_{source} is the measured virtual source size. Modifying Bergin’s formula for the beam standard deviation for non-normal incidence, see Section Appendix A, and substituting $\beta = \sigma_{\text{source}}/L$, we arrive at

$$\phi_x^2 = \underbrace{\left(\frac{d}{2\sqrt{3}}\right)^2}_{\text{geometric}} + \underbrace{\left(\frac{1}{\cos\theta} \frac{\sigma_s f}{\sqrt{3}L}\right)^2}_{\text{source size}} + \underbrace{\left(\frac{1}{\cos\theta} \frac{0.42\lambda f}{d \cos\theta}\right)^2}_{\text{diffraction}}, \quad (1)$$

as the beam standard deviation along the horizontal scanning direction, denoted x in figure 2.

ϕ_x corresponds to the beam standard deviation that is measured by scanning the beam over a sharp edge, however, as can be seen in figure 2 the beam is actually narrower than the measured quantity by $\phi = \phi_x \cos\theta$ due to non-normal incidence of the beam on the sample. We denote the beam standard deviation with lower case ϕ and the beam full width at half maximum (FWHM) as capital Φ . The FWHM is taken to be our measure of beamwidth and hence representative of resolution in a similar manner to previous work[20, 32, 33, 17]. We term Φ the *intrinsic beamwidth* and Φ_x the *projected beamwidth*. The resolving power of the instrument will depend both on the intrinsic beamwidth, and the orientation of features relative to the beam, with those perpendicular to the beam resolved the best and those parallel not resolved at all.

3.2. Optimisation

The optimisation procedure seeks the atom-optical parameters that maximise signal for a chosen target beamwidth. For a pinhole microscope, the mathematical optimum in working distance, f , lies at $f = 0$, but that limit is not useful experimentally. In the Cambridge-type SHeM, reducing f too far would compromise one of the central practical advantages of the geometry: a large depth of field together with straightforward sample manipulation. Our aim is therefore not to reach the formal zero-working-distance optimum, but to identify the best usable configuration for a sub-micron, large-working-distance instrument.

We choose a target intrinsic beamwidth of approximately $\Phi \sim 300$ nm for two reasons. First, this would make the Cambridge-type geometry competitive with the best reported beamwidths of Portland-type NAM. Second, previous theoretical work suggests that this length scale remains favourable for a pinhole instrument, rather than requiring active focusing such as a zone plate[26].

The optimisation requires a choice of working distance, f , from which the other parameters follow. We impose two practical constraints. First, we require a depth of field at least $\times 1000$ larger than the target beamwidth. Previous studies indicate that the effective depth of field in Cambridge-type SHeM extends approximately $\pm g$ from the design working distance, with $g \sim f/3$ for a retention of around $2/3$ of the signal level [29]. Second, we require sufficient space between the pinhole and the scattering plane, F , for bulk samples and straightforward sample manipulation. For a target beamwidth of $\Phi \sim 300$ nm this leads, after correcting for the $\theta = 45^\circ$ geometry, to a lower limit of roughly $f > 650 \mu\text{m}$. Imposing $F \sim 500 \mu\text{m}$ then gives a practical design value of $f \sim 710 \mu\text{m}$. Applying constrained optimisation to equation 1 in the same manner as Bergin (details in Appendix A) gives the optimum pinhole diameter and angular source size as

$$d_0 = \sqrt{6} \phi_x \quad (2)$$

$$\beta_0 = \frac{\sqrt{3}}{\sqrt{2}f} \left(\frac{\phi_x^2}{2} - \frac{a^2}{6\phi_x^2} \right)^{\frac{1}{2}}. \quad (3)$$

Here $a = 0.42\lambda d / \cos^2 \theta$, with $\lambda = 0.57 \text{ \AA}$ for room-temperature helium.

For a target intrinsic beam FWHM of approximately 300 nm, the constrained optimisation yields the design targets summarised in table 1, including an optimum pinhole diameter of order 440 nm and an optimum angular source size of order 2.2×10^{-4} rad. The fact that the optimised pinhole diameter exceeds the target intrinsic beamwidth is not contradictory: the optimisation is carried out in terms of the projected Gaussian beamwidth, for which the pinhole diameter contributes only one term in the overall quadrature sum of geometric, source-size and diffraction broadening.

For the chosen working distance, the optimised design predicts sub-micron performance, with geometric, source-size and diffraction terms all contributing materially to the overall beamwidth, rather than the resolution being dominated almost entirely by geometric broadening (table 1).

The optimisation also implies a substantial signal penalty relative to the earlier large-working-distance configuration. Reducing the pinhole diameter and increasing the source-pinhole distance both reduce the transmitted flux, while the final signal level also depends on the detector aperture and contrast mechanism. For this reason the signal cannot be predicted from geometry alone, and in practice it is more meaningful to estimate it by comparison with a known experimental configuration using the same source and detector[15, 19, 33]. Relative to that earlier configuration, the optimised design is expected to incur a large raw signal loss, of approximately one order of magnitude

before mitigation by detector-aperture redesign, which must be mitigated in the experimental realisation by redesign of the local scattering geometry and detector acceptance.

Quantity	Value
Target intrinsic beamwidth Φ	300 nm
Target projected beamwidth Φ_x	424 nm
Optimised pinhole diameter d_0	440 nm
Optimised angular source size β_0	2.2×10^{-4} rad
Design working distance f	0.71 mm
Design pinhole-sample spacing F	0.50 mm
Helium wavelength λ	0.57 \AA
Manufactured pinhole diameter d_0	470 nm
Predicted projected beamwidth Φ_x	470 nm
Predicted intrinsic beamwidth Φ	330 nm
Geometric contribution	68%
Source-size contribution	64%
Diffraction contribution	36%
Estimated raw signal penalty	$\sim \times 18$

Table 1: Optimised design targets and predicted performance for the high-resolution large-working-distance configuration. The intrinsic beamwidth is $\sqrt{2}$ smaller than the projected beamwidth owing to the 45° incidence geometry. Contribution percentages are expressed relative to the overall predicted beamwidth. The predicted beamwidths and contributions are based on the actual diameter of the manufactured pinhole.

4. Experimental Implementation and Design

The optimisation of Section 3 specifies the atom-optical requirements for sub-micron, large-working-distance operation, but realising that design in practice raises three distinct implementation challenges:

1. increasing the source-pinhole distance to reduce the angular source size,
2. reducing the working distance without losing practical sample access, and
3. compacting the local scattering geometry sufficiently to preserve useful detector acceptance despite the smaller pinhole-sample separation.

The experimental redesign was therefore organised around three corresponding hardware changes: a chamber geometry that allows the source distance to be varied over a larger range, a reduced working-distance sample region, and a miniaturised pinhole-plate that implements the compact pinhole-sample-detector geometry required by the optimisation. To enact these changes, a new sample chamber was designed and installed, a cross-sectional render of which is shown in figure 3, together with a newly designed defining optical element, the high-resolution pinhole-plate. In the Cambridge SHeM the pinhole-plate is mounted in the sample chamber and holds the pinhole membrane in place, while also defining the path from the sample to the detector and the local geometry of the scattering region.

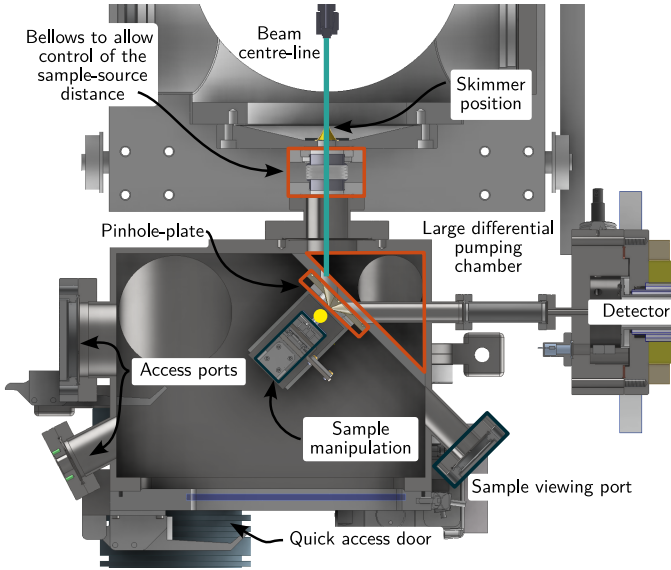


Figure 3: A cross-sectional render of the Cambridge SHeM, with a new sample chamber installed: the sample chamber is the large rectangular chamber in the lower left of the render. Key features of the new chamber are highlighted. The quick access door and the large number of access ports (3 more on the top of the chamber are not rendered) are usability improvements. The large differential pumping chamber decreases background, while the adjustable bellows, pinhole-plate, and viewing port enable the optical system changes to enable the high resolution imaging mode. The sample is mounted at the yellow dot in the centre of the render.

4.1. New sample chamber

The new rectangular chamber is split into two sub-chambers which maximises signal to noise through the reduction of background by an optimisation of the pumping speed in the differential chamber[25]. The chamber is designed to have ample space for extended sample manipulation, alternative pinhole-plate designs (such as that used by Radić et al.[34]), and other new sample environments, with a generous number of access ports on the side and top giving direct access to the sample area. The angular source size can be manipulated by changing the distance between the skimmer, which defines the source size, and the pinhole using the bellows highlighted in figure 3. A large range of source distances are possible, from a minimum of ~ 130 mm, to ~ 400 mm. The same $10\ \mu\text{m}$ nozzle and $100\ \mu\text{m}$ skimmer we used as the original Cambridge SHeM, meaning the virtual source size, $80\ \mu\text{m}$ FWHM at nozzle pressures of ≈ 75 bar, is the same as previously reported[32]. For the high-resolution configuration reported here, the source–pinhole distance was set to $L = 385 \pm 20$ mm, corresponding to a realised angular source size of $\beta = 2.18 \pm 0.11 \times 10^{-4}$ rad. This places the implemented source geometry in close agreement with the optimised requirement identified in Section 3.

4.2. New pinhole-plate optical element

The pinhole-plate is the defining optical element of the Cambridge-type SHeM in the immediate sample region[35]. The top panel of figure 4 shows a cross section of a pinhole plate, it consists of a mount for a silicon nitride membrane into which is

milled the pinhole, a detector aperture which collects the scattered atoms, as well as pathways from the differential source and to the detector. The pinhole plate mounts to the wall of the sample chamber and isolates the source side of the instrument from the detector side of the instrument. In terms of the atom optics it fixes the local scattering geometry of the instrument: it sets the working distance, determines the solid angle subtended by the detector aperture, and establishes the relative positions of the pinhole, sample and detector. To realise our optimised system the pinhole and detector aperture need to be brought closer together, while simultaneously increasing the solid angle of the detector aperture. Therefore a miniaturisation of the pinhole plate features was required. A cross-sectional diagram of a generic pinhole plate and a to scale cross-section of the defining apertures of the new high-resolution pinhole-plate, manufactured by 3D printing in plastic[36], is shown in figure 4. With the reduced working distance of $f \approx 0.71$ mm the pinhole position becomes close to the centre of the detector aperture, ~ 1.5 mm, which that aperture is also enlarge relative to the previous design. The new working distance is approximately one quarter of that used previously with the Cambridge SHeM, although still around one to one-and-a-half orders of magnitude larger than the short-working-distance Portland-type NAM[20].

The miniaturised design made the membrane scaffold itself a critical design constraint. Commercially available pinholes, or the standard Agar Scientific membranes used previously¹, have lateral dimensions of order 3 mm. These would occupy too much of the compact sample region to leave sufficient space for the detector aperture. For this reason a custom square silicon nitride membrane, with scaffold approximately 1 mm wide were used, allowing a corresponding miniaturisation of the pinhole-plate assembly. The new membrane scaffold is shown to scale in figure 4 and final milled structure are shown directly in the SEM micrographs of figure 5. After mounting the membrane onto the pinhole-plate with vacuum leak sealant, the assembly was sputter-coated with gold and transferred to a FIB-SEM² for focused ion beam milling of the final pinhole. The realised pinhole diameter after milling was $d = 470$ nm, slightly larger than the optimised target value of approximately 440 nm but still within the regime required for sub-micron performance.

The enlarged detector aperture in the pinhole-plate redesign was also used to recover as much contrast-bearing signal as possible after the substantial signal losses imposed by the smaller pinhole and increased source–pinhole distance. In the new design, the solid angle subtended by the detector aperture, Ω , is increased from 0.094 sr in the previous configuration to 1.44 sr, an increase by a factor of approximately 15. For the diffuse topographic contrast mode used here, previous work has shown that increasing detector solid angle can improve contrast-to-noise performance without a corresponding penalty in image quality, even though a larger fraction of the scattering distribution is averaged[33]. In the present case this corresponds to

¹Agar Scientific Ltd. silicon nitride membranes in support frames compatible with 3mm TEM holders: <https://www.agarscientific.com/silicon-nitride-membranes-200-181-m-substrate-thickness>.

²FEI Helios NanoLab 600i with a Ga⁺ beam.

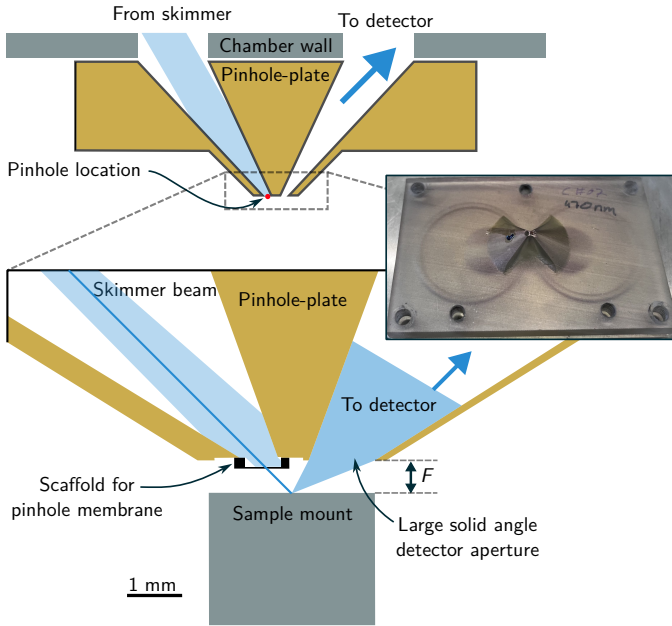


Figure 4: Top, schematic of a pinhole plate (orange) in the Cambridge SHeM, the pinhole plate is mounted to the sample chamber wall and separates the incoming source chambers from the detector chamber, it defines the path of the atoms from the source to the pinhole and from the detector aperture to the detector chamber. Bottom, a to-scale cross-sectional view of the tip of the high-resolution pinhole-plate, showing the scaffold for the pinhole membrane and the large solid angle detector aperture. The inset shows the realised 3D-printed assembly with the pinhole membrane installed.

an estimated contrast-to-noise benefit equivalent to roughly an eightfold increase in signal level[33].

The enlarged detector acceptance does not fully compensate the signal losses associated with the reduction in pinhole diameter and the increased source–pinhole distance, but it does remain practical. The net effect is a reduction in signal by a factor of approximately 2.25 relative to the earlier configuration, but this was found to be acceptable in practice through a combination of moderately increased measurement time and tolerance of a slightly reduced signal-to-noise ratio. The use of a larger aperture to compensate for a smaller beam is, however, contrast-mechanism specific: very large apertures still produce good diffuse topographic contrast[37], which is the imaging mode most relevant to the samples presented here. It is possible the resulting design may be less well suited to forms of contrast that depend more strongly on angular selectivity, such as diffraction contrast[38, 5].

5. Measured beamwidth

To measure the beamwidth, we scan over a sharp edge on a standard copper TEM grid³ and monitor the detected helium signal, as demonstrated in figure 6. The beamwidth was extracted from the measured signal by fitting an error function and

³Square Pattern 50 Mesh TEM Support Grids, from Agar Scientific www.agarscientific.com/tem/grids-agar/square-50-mesh-tem-support-grids.

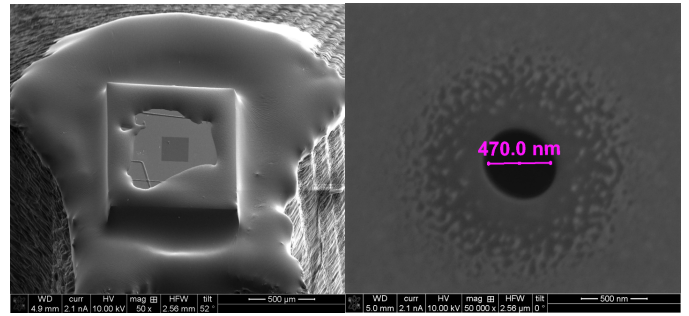


Figure 5: SEM micrographs of the FIB-milled pinhole in the Si-N membrane. The custom 1 mm square membrane scaffold is visible, demonstrating the miniaturised support structure required by the compact pinhole-plate geometry. The membrane is mounted into the pinhole-plate prior to FIB milling.

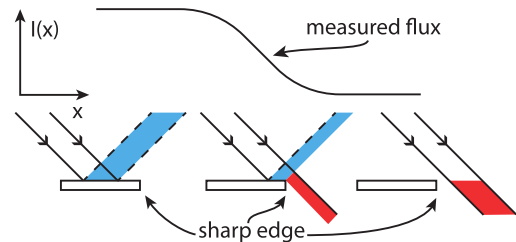


Figure 6: Scanning across a step edge with steps smaller than the beam width will result in the detected helium flux, $I(x)$ shown in blue, changing as a greater fraction of the beam falls off the edge, in red.

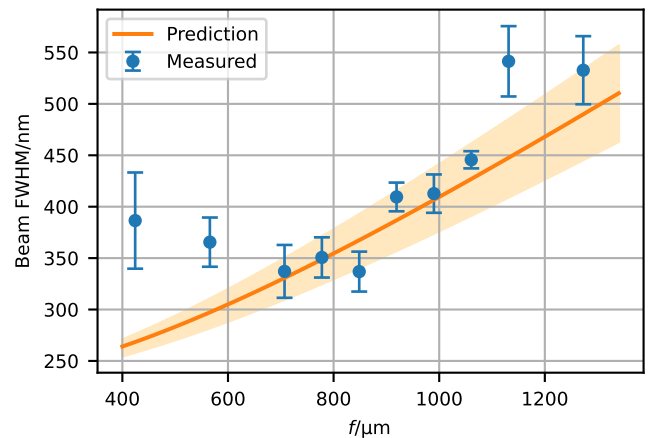


Figure 7: Beamwidth measurements, plotted as the intrinsic beamwidth ϕ , taken across a wire edge provided by a copper TEM grid as a function of the working distance f . Two different edges were used for each measurement and a weighted average taken. The predicted beamwidth uses equation 1 and the confidence interval represents one standard deviation in the predicted value based on the uncertainty in the source size σ_s [32]. Working distances are all measured to $\pm 25 \mu\text{m}$.

extracting the associated standard deviation. Figure 7 shows the measured intrinsic beamwidths plotted as a function of the working distance, as well as a predicted beamwidth from equation 1. The measured beamwidths follow the expected trend, with beamwidths near and slightly larger than the design working distance agreeing with the prediction. The smallest measured beamwidth was 340 ± 20 nm at a working distance of $f = 850 \pm 25$ μm . We can see from figure 7 that we maintain a narrow beamwidth over a significant range of working distances, $\sim 550 - 1100$ μm , satisfying our requirement for a large depth of field. For working distances significantly larger and smaller than the design distance, we see divergence from the expected beamwidth, we attribute the divergence to decreased signal to noise when the instrument is used away from its design geometry. The observation is consistent with our previous results that demonstrated an ‘effective depth of field’ for pinhole SHeM of $\sim \pm f/3$ [29].

6. High resolution imaging

Four example samples were chosen to explore the capabilities of the new high resolution imaging mode, these are all presented in figure 8.

Figure 8 (b) shows a micrograph of *Pseudomonas aeruginosa* which has formed a bacterial biofilm and exhibits very high topographic detail, with strong contrast. In particular the complex pattern of the formaldehyde crystals, recognised by their string-like appearance, easily made out. Figure 8 (d) shows a micrograph of isolated *Clostridioides difficile* (*C. diff*) bacteria, these appear as small rod shapes, and are generally < 1 μm in diameter, therefore it would not have been possible to resolve them with our previous configuration – or any other large working distance pinhole helium microscope[39]. Both bacterial specimens were fixed with formaldehyde.

Figure 8 (c) shows micrographs of mechanically eroded synthetic diamond imaged with the old configuration (left) and the new optimised configuration (right). The eroded diamond has a strongly faceted surface arising from chunks of the material being removed during the erosion process. With the previous SHeM setup only being able to resolve some of the largest grooves and struggling to visualise any detail.

The final sample was a reusable PPE face mask fabric and presents a particularly difficult structure to image due to being both insulating and having features as large perpendicular to the image plane as within it. The SHeM micrograph in figure 8 (a) resolves the fabric filaments deep into the material as well as at the surface, demonstrating that we have been successful in maintaining the impressive depth of the field of the Cambridge-type SHeM in the sub-micron beamwidth regime.

7. Outlook

The present work describes the optimisation of and experimental advances in large-working-distance pinhole SHeM as a viable sub-micron microscopy platform. The achieved intrinsic beamwidth of 340 nm narrows much of the gap between the

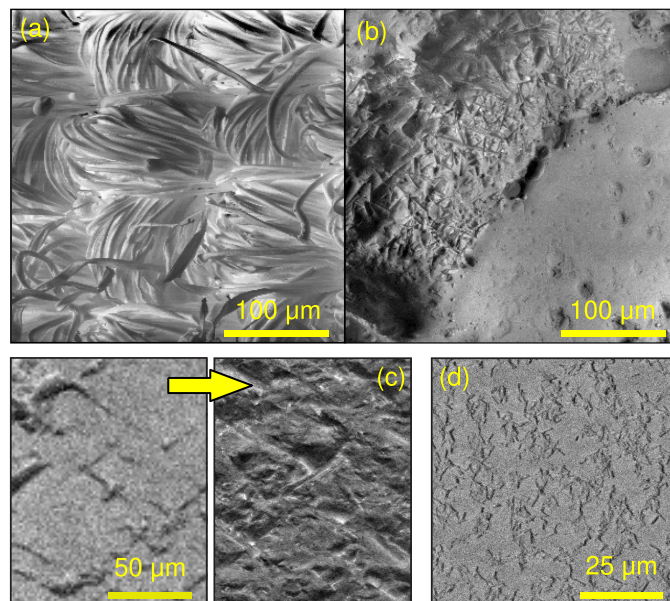


Figure 8: Example high-resolution SHeM micrographs demonstrating a large depth of field (top row) and high fidelity (bottom row). (a) Reusable PPE face mask fabric provided by L. Fruk (Chemical Engineering Department, University of Cambridge). (b) Formaldehyde-fixed *Pseudomonas aeruginosa* bacterial biofilm on a generic glass slide. (c) Polycrystalline diamond from Element Six, eroded by T. Cowie with 100 μm silicon carbide particles [40]. The left panel shows the surface prior to resolution improvements; the right panel (c) shows the significant increase in surface detail following the improvements. (d) Isolated *Clostridioides difficile* (*C. diff*) bacteria provided by L. Dawson (London School of Hygiene and Tropical Medicine, LSHTM) [41], grown directly on round polymer coverslips (Thermo Fisher 174950). Panels (a) and (b) were acquired with a pixel size of 1.00 μm , while panels (c) and (d) were acquired with a pixel size of 0.50 μm .

Cambridge-type geometry and the best reported short-working-distance Portland-type NAM performance, while retaining the practical advantages of larger working distance, including improved sample access, tolerance of topography, and a useful depth of field. In microscopy terms, this is the central result: large-working-distance SHeM can now operate in a resolution regime that begins to make fuller use of its non-destructive and surface-sensitive character.

An important consequence of the present optimisation is that the beamwidth is no longer dominated almost entirely by simple geometric broadening. Instead, geometric, and source-size contributions are now very similar, indicating an optimised regime and that further gains from passive optimisation of the same architecture are likely to be limited. The diffraction term remains the smallest, but cannot uniquely be tuned due to the fixed helium wavelength. Some additional improvement may still be possible by trading working distance against resolution, for example by moving towards normal incidence or reducing the pinhole–sample separation further, but such changes would come at the cost of reduced usability and reduced tolerance of sample topography. Therefore, the present work represents not only an improvement in beamwidth, but it clarifies the current technical frontier. Within the pinhole-collimated geometry, further substantial gains are likely to require a complete rethinking of the instrumental design, rather than further evolution of

the current design paradigm. In particular, active focusing approaches such as Fresnel zone plates remain the most promising route if helium microscopy is to move substantially beyond the performance demonstrated here[42]. The present results therefore help define the performance envelope of optimised large-working-distance pinhole SHeM and provide a useful benchmark against which future focused-beam approaches can be assessed.

At the same time, the sub-micron regime already opens up a much broader range of measurements than was previously accessible to large-working-distance SHeM. For topographic imaging, it extends the usefulness of the technique for delicate and insulating specimens whose relevant structure lies below the micron scale. For atom-diffraction and spot-profile measurements, it makes it more realistic to probe smaller individual domains and heterogeneous regions, including exfoliated and spatially non-uniform 2D systems, for which micron-scale beam sizes were previously a substantial limitation[5, 43]. More broadly, the work shows that the practical advantages of the Cambridge-type geometry need not be confined to low-resolution operation, and that helium microscopy can increasingly be considered not simply as a specialised surface-science instrument, but as a flexible microscopy platform with growing relevance for challenging real-world specimens.

Acknowledgements

The work was supported by EPSRC grant EP/R008272/1. The work was performed in part at CORDE, the Collaborative R&D Environment established to provide access to physics related facilities at the Cavendish Laboratory, University of Cambridge and EPSRC award EP/T00634X/1. SML acknowledges support from IAA award EP/X525686/1. The authors acknowledge support from Ionoptika Ltd. We thank Dr L Dawson of the London School for Tropical Medicine for the biofilm samples, T Cowie and Element Six for the eroded diamond samples, and Dr L. Fruk from the University of Cambridge Chemical Engineering department for the fabric face mask sample.

Data availability

Raw and processed data are available upon reasonable request.

References

- [1] R. F. Egerton, P. Li, M. Malac, Radiation damage in the TEM and SEM, *Micron* 35 (6) (2004) 399–409. doi:10.1016/j.micron.2004.02.003.
- [2] M. T. Postek, A. E. Vladár, Does your SEM really tell the truth?—how would you know? part 1, *Scanning* 35 (6) (2013) 355–361. doi:https://doi.org/10.1002/sca.21075.
- [3] A. S. Palau, S. D. Eder, G. Bracco, B. Holst, Neutral helium atom microscopy, *Ultramicroscopy* 251 (2023) 113753. doi:10.1016/j.ultramicro.2023.113753.
- [4] S. D. Eder, A. Fahy, M. G. Barr, J. R. Manson, B. Holst, P. C. Dastoor, Sub-resolution contrast in neutral helium microscopy through facet scattering for quantitative imaging of nanoscale topographies on macroscopic surfaces, *Nature Communications* 14 (1) (2023) 904. doi:10.1038/s41467-023-36578-x.
- [5] N. A. von Jeinsen, S. M. Lambrick, M. Bergin, A. Radić, B. Liu, D. Seremet, A. P. Jardine, D. J. Ward, 2d helium atom diffraction from a microscopic spot, *Physical Review Letters* 131 (23) (2023) 236202. doi:10.1103/PhysRevLett.131.236202.
- [6] B. Holst, G. Alexandrowicz, N. Avidor, G. Benedek, G. Bracco, W. E. Ernst, D. Farías, A. P. Jardine, K. Lefmann, J. R. Manson, R. Marquardt, S. M. Artés, S. J. Sibener, J. W. Wells, A. Tamtögl, W. Allison, Material properties particularly suited to be measured with helium scattering: selected examples from 2d materials, van der waals heterostructures, glassy materials, catalytic substrates, topological insulators and superconducting radio frequency materials, *Physical Chemistry Chemical Physics* 23 (13) (2021) 7653–7672. doi:10.1039/D0CP05833E.
- [7] C. J. Hatchwell, M. Bergin, B. Carr, M. G. Barr, A. Fahy, P. C. Dastoor, Measuring scattering distributions in scanning helium microscopy, *Ultramicroscopy* 260 (2024) 113951. doi:10.1016/j.ultramicro.2024.113951.
- [8] R. Flatabø, S. D. Eder, T. Reisinger, G. Bracco, P. Baltzer, B. Samelin, B. Holst, Reflection imaging with a helium zone plate microscope, *Ultramicroscopy* 261 (2024) 113961. doi:10.1016/j.ultramicro.2024.113961.
- [9] M. Barr, A. Fahy, A. Jardine, J. Ellis, D. Ward, D. MacLaren, W. Allison, P. Dastoor, A design for a pinhole scanning helium microscope, *Nuclear Instruments and Methods in Physics Research Section B: Beam Interactions with Materials and Atoms* 340 (2014) 76–80. doi:10.1016/j.nimb.2014.06.028.
- [10] G. Bhardwaj, K. R. Sahoo, R. Sharma, P. Nath, P. R. Shirhatti, Neutral-atom-scattering-based mapping of atomically thin layers, *Physical Review A* 105 (2) (2022) 022828. doi:10.1103/PhysRevA.105.022828.
- [11] P. Witham, E. Sánchez, A simple approach to neutral atom microscopy, *Review of Scientific Instruments* 82 (10) (2011) 103705. doi:10.1063/1.3650719.
- [12] G. Bhardwaj, P. R. Shirhatti, Contrast inversion in neutral-atom microscopy using atomic cluster beams, *Physical Review A* 107 (6) (2023) 062813. doi:10.1103/PhysRevA.107.062813.
- [13] A. Radic, N. v. Jeinsen, V. Perez, K. Wang, M. Lin, B. Liu, Y. Zhu, I. Sami, K. Watanabe, T. Taniguchi,

- D. Ward, A. Jardine, A. Rao, M. Chhowalla, S. Lambrick, Measuring vacancy-type defect density in monolayer MoS₂ (2025). arXiv:2409.18637 [physics], doi:10.48550/arXiv.2409.18637.
- [14] T. A. Myles, S. D. Eder, M. G. Barr, A. Fahy, J. Martens, P. C. Dastoor, Taxonomy through the lens of neutral helium microscopy, *Scientific Reports* 9 (1) (2019) 2148. doi:10.1038/s41598-018-36373-5.
- [15] S. M. Lambrick, L. Vozdecký, M. Bergin, J. E. Halpin, D. A. MacLaren, P. C. Dastoor, S. A. Przyborski, A. P. Jardine, D. J. Ward, Multiple scattering in scanning helium microscopy, *Applied Physics Letters* 116 (6) (2020) 061601. doi:10.1063/1.5143950.
- [16] M. Bergin, W. Roland-Batty, C. J. Hatchwell, T. A. Myles, J. Martens, A. Fahy, M. Barr, W. J. Belcher, P. C. Dastoor, Standardizing resolution definition in scanning helium microscopy, *Ultramicroscopy* 233 (2022) 113453. doi:10.1016/j.ultramic.2021.113453.
- [17] S. D. Eder, T. Reisinger, M. M. Greve, G. Bracco, B. Holst, Focusing of a neutral helium beam below one micron, *New Journal of Physics* 14 (7) (2012) 073014. doi:10.1088/1367-2630/14/7/073014.
- [18] S. D. Eder, A. Salvador Palau, T. Kaltenbacher, G. Bracco, B. Holst, Velocity distributions in microskimmer supersonic expansion helium beams: High precision measurements and modeling, *Review of Scientific Instruments* 89 (11) (2018) 113301. doi:10.1063/1.5044203.
- [19] M. Bergin, D. J. Ward, S. M. Lambrick, N. A. von Jeinsen, B. Holst, J. Ellis, A. P. Jardine, W. Allison, Low-energy electron ionization mass spectrometer for efficient detection of low mass species, *Review of Scientific Instruments* 92 (7) (2021) 073305. doi:10.1063/5.0050292.
- [20] P. J. Witham, E. J. Sánchez, Increased resolution in neutral atom microscopy, *Journal of Microscopy* 248 (3) (2012) 223–227. doi:10.1111/j.1365-2818.2012.03665.x.
- [21] M. Koch, S. Rehbein, G. Schmahl, T. Reisinger, G. Bracco, W. E. Ernst, B. Holst, Imaging with neutral atoms—a new matter-wave microscope, *Journal of Microscopy* 229 (1) (2008) 1–5. doi:10.1111/j.1365-2818.2007.01874.x.
- [22] S. D. Eder, X. Guo, T. Kaltenbacher, M. M. Greve, M. Källäne, L. Kipp, B. Holst, Focusing of a neutral helium beam with a photon-sieve structure, *Physical Review A* 91 (4) (2015) 043608. doi:10.1103/PhysRevA.91.043608.
- [23] R. Flatabø, M. M. Greve, S. D. Eder, M. Källäne, A. S. Palau, K. K. Berggren, B. Holst, Atom sieve for nanometer resolution neutral helium microscopy, *Journal of Vacuum Science & Technology B* 35 (6) (2017) 06G502. doi:10.1116/1.4994330.
- [24] C. Zhao, S. M. Lambrick, N. A. v. Jeinsen, Y. Yuan, X. Zhang, A. Radić, D. J. Ward, J. Ellis, A. P. Jardine, A multi-detector neutral helium atom microscope, *Vacuum* 234 (2025) 114006. doi:10.1016/j.vacuum.2024.114006.
- [25] A. Fahy, M. Barr, J. Martens, P. C. Dastoor, A highly contrasting scanning helium microscope, *Review of Scientific Instruments* 86 (2) (2015) 023704. doi:10.1063/1.4907539.
- [26] M. Bergin, D. J. Ward, J. Ellis, A. P. Jardine, A method for constrained optimisation of the design of a scanning helium microscope, *Ultramicroscopy* (2019) 112833doi:10.1016/j.ultramic.2019.112833.
- [27] A. Salvador Palau, G. Bracco, B. Holst, Theoretical model of the helium zone plate microscope, *Physical Review A* 95 (1) (2017). doi:10.1103/PhysRevA.95.013611.
- [28] D. P. DePonte, S. D. Kevan, F. S. Patton, Brightness of micronozzle helium source, *Review of Scientific Instruments* 77 (5) (2006) 055107. doi:10.1063/1.2198813.
- [29] S. M. Lambrick, M. Bergin, A. P. Jardine, D. J. Ward, A ray tracing method for predicting contrast in neutral atom beam imaging, *Micron* 113 (2018) 61–68. doi:10.1016/j.micron.2018.06.014.
- [30] A. S. Palau, G. Bracco, B. Holst, Theoretical model of the helium pinhole microscope, *Physical Review A* 94 (6) (2016). doi:10.1103/PhysRevA.94.063624.
- [31] J. Kelsall, A. Radić, J. Ellis, D. J. Ward, A. P. Jardine, Minimizing interference in low-pressure supersonic beam sources, *The Journal of Chemical Physics* 162 (9) (2025) 094304. doi:10.1063/5.0247870.
- [32] M. Bergin, Instrumentation and contrast mechanisms in scanning helium microscopy, Ph.D. thesis, Fitzwilliam College, University of Cambridge (2018). doi:10.17863/CAM.37853.
- [33] Sam M. Lambrick, The formation of contrast in scanning helium microscopy, Ph.D. thesis, Hughes Hall, University of Cambridge (2021). doi:10.17863/CAM.83463.
- [34] A. Radić, S. M. Lambrick, N. A. von Jeinsen, A. P. Jardine, D. J. Ward, 3d surface profilometry using neutral helium atoms, *Applied Physics Letters* 124 (20) (2024) 204101. doi:10.1063/5.0206374.
- [35] M. Bergin, T. A. Myles, A. Radić, C. J. Hatchwell, S. M. Lambrick, D. J. Ward, S. D. Eder, A. Fahy, M. Barr, P. C. Dastoor, Complex optical elements for scanning helium microscopy through 3d printing, *Journal of Physics D: Applied Physics* 55 (9) (2021) 095305. doi:10.1088/1361-6463/ac3a3e.

- [36] A. Radić, S. M. Lambrick, S. Rhodes, D. J. Ward, On the application of components manufactured with stereolithographic 3d printing in high vacuum systems, *Vacuum* 232 (2025) 113809. doi:10.1016/j.vacuum.2024.113809.
- [37] S. M. Lambrick, M. Bergin, D. J. Ward, M. Barr, A. Fahy, T. Myles, A. Radić, P. C. Dastoor, J. Ellis, A. P. Jardine, Observation of diffuse scattering in scanning helium microscopy, *Physical Chemistry Chemical Physics* 24 (43) (2022) 26539–26546. doi:10.1039/D2CP01951E.
- [38] M. Bergin, S. M. Lambrick, H. Sleath, D. J. Ward, J. Ellis, A. P. Jardine, Observation of diffraction contrast in scanning helium microscopy, *Scientific Reports* 10 (1) (2020) 1–8. doi:10.1038/s41598-020-58704-1.
- [39] N. A. von Jeinsen, D. J. Ward, M. Bergin, S. M. Lambrick, D. M. Williamson, R. M. Langford, L. F. Dawson, V. Rana, S. Shivaswamy, X. Zhou, M. Mikes, V. D. Gordon, B. W. Wren, K. A. Brown, P. C. Dastoor, Surface visualisation of bacterial biofilms using neutral atom microscopy, *Journal of Microscopy* 301 (1) (2026) 107–115. doi:10.1111/jmi.70038.
- [40] A. J. Henderson, The Solid Particle Erosion of Polycrystalline Diamond at High and Low Temperatures, Ph.D. thesis, Robinson College, University of Cambridge (May 2020). doi:10.17863/CAM.51694.
- [41] L. F. Dawson, J. Peltier, C. L. Hall, M. A. Harrison, M. Derakhshan, H. A. Shaw, N. F. Fairweather, B. W. Wren, Extracellular DNA, cell surface proteins and c-di-GMP promote biofilm formation in *Clostridioides difficile*, *Scientific Reports* 11 (1) (2021) 3244. doi:10.1038/s41598-020-78437-5.
- [42] R. Flatabø, S. D. Eder, T. Reisinger, G. Bracco, P. Baltzer, B. Samelin, B. Holst, Reflection imaging with a helium zone plate microscope (2023). arXiv:2308.11749[physics], doi:10.48550/arXiv.2308.11749.
- [43] A. Radic, N. von Jeinsen, K. Wang, Y. Zhu, I. Sami, V. Perez, D. Ward, A. Jardine, M. Chhowalla, S. Lambrick, Defect density quantification in monolayer MoS₂ using helium atom micro-diffraction (2024). doi:10.48550/arXiv.2409.18637.

Appendix A. Constrained optimisation for non-normal incidence

The formula for the beam standard deviation, ϕ , derived by Bergin is

$$\phi^2 = \underbrace{\left(\frac{d}{2\sqrt{3}}\right)^2}_{\text{geometric}} + \underbrace{\left(\frac{\beta f}{\sqrt{3}}\right)^2}_{\text{source size}} + \underbrace{\left(\frac{0.42\lambda f}{d}\right)^2}_{\text{diffraction}}, \quad (\text{A.1})$$

where d is the pinhole diameter, f is the working distance, β is the angular source size and λ is the wavelength of the helium atoms. Modifications are required in order to apply equation A.1 to a non-normal incidence configuration, such as the Cambridge SHeM. We must also consider that the pinhole in the Cambridge SHeM is mounted parallel to the xy scanning axes, and therefore at an angle to the incident beam, as shown in figure A.9. With non-normal incidence the beamwidth may be different in the two principle scanning axes, we consider the horizontal scanning axis, that which is in plane with the incoming helium beam and follows the arrow in figure A.9. We will consider the three terms in equation A.1 with respect to measuring a beamwidth projected into the horizontal scanning axis, which we shall label as the x -axis.

geometric As the pinhole is in the same plane as the scanning axis of interest, then the geometric projection of the pinhole is unchanged.

source A beamwidth measured parallel to the scanning axis will be observed to be $1/\cos\theta$ larger than it actually is.

diffraction As with the source size, the angle between the beam and the scanning axis will introduce a factor of $1/\cos\theta$. In addition, because the beam is arriving at an angle to the pinhole, the effective width of the pinhole is reduced by a factor $\cos\theta$.

Thus the beam standard deviation as measured in the scanning plane, ϕ_x , is

$$\phi_x^2 = \left(\frac{d}{2\sqrt{3}}\right)^2 + \left(\frac{1}{\cos\theta} \frac{\beta f}{\sqrt{3}}\right)^2 + \left(\frac{1}{\cos\theta} \frac{0.42\lambda f}{d \cos\theta}\right)^2. \quad (\text{A.2})$$

Define the constant $a = 0.42\lambda f / \cos^2\theta$. Following the formulation by Bergin the Lagrange multiplier is

$$\mathcal{L} = \gamma d^2 \beta^2 - \Lambda \left[\sqrt{\left(\frac{d}{2\sqrt{3}}\right)^2 + \left(\frac{\beta f}{\sqrt{3} \cos\theta}\right)^2} + \left(\frac{a}{d}\right)^2 - \phi_x \right], \quad (\text{A.3})$$

which must be minimised.

$$\frac{\partial \mathcal{L}}{\partial \beta} = 2\gamma d^2 \beta - \frac{\Lambda}{\phi_x} \frac{2\beta f^2}{3} \quad (\text{A.4})$$

$$\Rightarrow \frac{\Lambda}{\phi_x} = \frac{3\gamma d^2}{f^2} \quad (\text{A.5})$$

$$\frac{\partial \mathcal{L}}{\partial d} = 2\gamma \beta^2 d - \frac{\Lambda}{\phi_x} \left(\frac{d}{12} - \frac{a^2}{d^3} \right) \quad (\text{A.6})$$

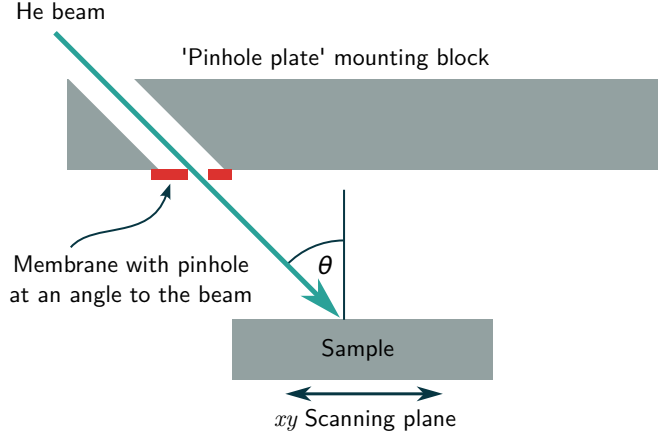


Figure A.9: In the Cambridge SHeM the pinhole is mounted on a ‘pinhole plate’. The pinhole plate is parallel to the scanning plane of the sample manipulators, and therefore for non-zero θ the pinhole is at an angle to the incident helium beam.

as for normal incidence.

$$\frac{3\gamma d_0^2}{f^2} = \frac{2\gamma \beta_0^2 d_0^4}{\frac{d_0^4}{12} - a^2} \quad (\text{A.7})$$

$$\Rightarrow \frac{2f^2 \beta_0^2}{3} = \frac{d_0^2}{12} - \frac{a^2}{d_0^2} \quad (\text{A.8})$$

Which gives the constrained optimisation values for pinhole size and virtual source size as

$$d_0 = \sqrt{6}\phi_x \quad (\text{A.9})$$

$$\beta_0 = \frac{\sqrt{3}}{\sqrt{2}f} \left(\frac{\phi_x^2}{2} - \frac{a^2}{6\phi_x^2} \right)^{\frac{1}{2}} \quad (\text{A.10})$$

which is the same as for normal incidence with a re-definition of the constant a .

Appendix B. Extra figures

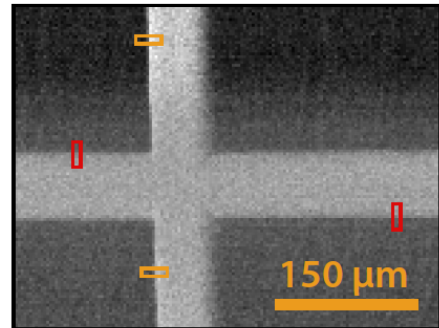


Figure B.10: SHeM micrograph of a standard TEM grid, with the location of the line scans performed to measure resolution highlighted.